Opto-Electronic Advances

Original Article

2022, Vol. 5, No. 8

DOI: 10.29026/oea.2022.200100

Polarization-switchable plasmonic emitters based on laser-induced bubbles

Jianjun Chen[1,2,3,4,5]* and Fengyuan Gan[2]

Owing to weak light-matter interactions in natural materials, it is difficult to dynamically tune and switch emission polarization states of plasmonic emitters (or antennas) at nanometer scales. Here, by using a control laser beam to induce a bubble (n=1.0) in water (n=1.333) to obtain a large index variation as high as $|\Delta n|$=0.333, the emission polarization of an ultra-small plasmonic emitter (~0.4λ^2) is experimentally switched at nanometer scales. The plasmonic emitter consists of two orthogonal subwavelength metallic nanogroove antennas on a metal surface, and the separation of the two antennas is only s_x=120 nm. The emission polarization state of the plasmonic emitter is related to the phase difference between the emission light from the two antennas. Because of a large refractive index variation ($|\Delta n|$=0.333), the phase difference is greatly changed when a microbubble emerges in water under a low-intensity control laser. As a result, the emission polarization of the ultra-small plasmonic emitter is dynamically switched from an elliptical polarization state to a linear polarization state, and the change of the degree of linear polarization is as high as $\Delta\gamma$≈0.66.

Keywords: plasmonic emitters; nanometer scales; polarization manipulation; dynamical switching; bubbles

Chen JJ, Gan FY. Polarization-switchable plasmonic emitters based on laser-induced bubbles. *Opto-Electron Adv* **5**, 200100 (2022).

Introduction

Surface plasmon polaritons (SPPs) with subwavelength field confinements can significantly shrink the sizes of photonic devices and improve integration densities of photonic integrated circuits[1–5]. However, the inherent Ohmic loss in metallic nanostructures is a major obstacle, limiting the practical applications of plasmonic devices[6–9]. Ultra-compact plasmonic emitters and receivers, which are an analog of microwave and radio-wave emitters and receivers, can be used to realize inter-chip optical communications between different photonic devices and different photonic chips[10–15]. By using inter-chip optical communications, the obstacle of the inherent Ohmic loss in metallic nanostructures can be overcome[13,15].

Up to now, a variety of plasmonic antennas were proposed to realize plasmonic emitters and receivers, including nanorod antennas[16,17], slot antennas[18–20], V- (or U-) shaped antennas[21,22], Yagi-Uda antennas[23–25], and so on. Most of these plasmonic antennas[18,21–24] were designed to control emission directions, greatly increasing the collection efficiencies of these plasmonic emitters. Recently, some works proposed to design plasmonic antennas to tailor emission polarization states, which provided new degrees of freedom in information encoding and increased communication capacity in inter-chip optical communications[26]. For example, by using Au nanoparticle antennas, the emission polarization of a dipole located at the antennas was tailored in theory[27]. By designing an orthogonal elongated nanorod and

[1]Department of Physics and Applied Optics Beijing Area Major Laboratory, Beijing Normal University, Beijing 100875, China; [2]State Key Laboratory for Mesoscopic Physics, School of Physics, Peking University, Beijing 100871, China; [3]Peking University Yangtze Delta Institute of Optoelectronics, Nantong 226010, China; [4]Frontiers Science Center for Nano-optoelectronics & Collaborative Innovation Center of Quantum Matter, Peking University, Beijing 100871, China; [5]Collaborative Innovation Center of Extreme Optics, Shanxi University, Taiyuan 030006, China.
*Correspondence: JJ Chen, Email: jjchern@bnu.edu.cn

Received: 30 December 2020; Accepted: 9 March 2021; Published online: 27 May 2022

complementary nanoslit antennas, the polarization control of free-space incident light was theoretically predicted[28]. By designing a metallic nanogroove antenna with a tilted angle on a gold film, emission light coming from an SPP waveguide mode was rotated in experiments[13]. Recently, Chen's group designed metasurface-based emitters on a two-dimensional plasmonic ridge waveguide, and the emission polarization of these metasurface-based emitters was experimentally tailored in both spectral and spatial domains at will[15].

Because of subwavelength field confinements of plasmonic antennas, the sizes of these plasmonic emitters were smaller than wavelengths. These subwavelength plasmonic emitters could significantly increase the integration densities of photonic chips[15]. However, in such a small device size ($<0.6\lambda^2$), it is difficult to dynamically tune and switch the emission polarization of these ultra-small plasmonic emitters owing to weak light-matter interactions in natural materials[29–34] and short interaction lengths (≤ device size). Herein, λ is a vacuum wavelength. As far as we know, polarization-switchable plasmonic emitters at nanometer scales have not been reported. Usually, to obtain large dynamic tuning ranges in active plasmonic devices[30–34], a large device size was required. For example, to efficiently switching (or modulating) optical signals, the sizes of plasmonic switchers (or modulators) were greater than 10 μm by using electro-optical[33,34], magneto-optical[32], and all-optical[30] methods. Therefore, it is still a great challenge to efficiently tune and switch the emission polarization of ultra-small plasmonic emitters at nanometer scales.

Design and principle

In the letter, we propose to use a control laser to induce a bubble in water to dynamically switch the emission polarization of an ultra-small plasmonic emitter at nanometer scales. Under a low control intensity, an index variation brought about by the laser-induced bubble effect can reach up to 0.333[4,35,36]. This index variation is much greater than those ($|\Delta n|\leq 0.06$) induced by electro-optical[33,34,37,38], thermo-optical[39,40], magneto-optical[32,41], and all-optical [29,42–44] tuning methods. Our designed plasmonic emitter (size ~$0.4\lambda^2$) consists of two orthogonal subwavelength metallic nanogroove antennas on a metal surface, and the separation of the two antennas is only s_x=120 nm. The ultra-small plasmonic emitter exhibits two different emission polarization states (linear polarization state and circular polarization state) when the plasmonic emitter is covered by different media with refractive indices of n=1.333 and 1.0. By using a control laser beam to induce a bubble (n=1.0) in water (n=1.333)[4,35,36], the emission polarization of the plasmonic emitter is dynamically switched from an elliptical polarization state to a linear polarization state in experiments.

The polarization-switching emitter consists of two orthogonal subwavelength metallic nanogroove antennas on a metal surface, as shown in Fig. 1(a). The metal surface is covered by a medium with a refractive index of n. An SPP mode confined on the metal surface propagates along the x-axis, and it then excites the resonant mode in the nanogroove antenna under a resonant condition[13]. Our previous works show that the emission polarization from the nanogroove antenna can be rotated by tilting the angle of the nanogroove antenna[13,15]. For two orthogonal nanogroove antennas on the metal surface (Fig. 1(a)), the polarization orientations of the emission light from the two nanogroove antennas are orthogonal[13]. The

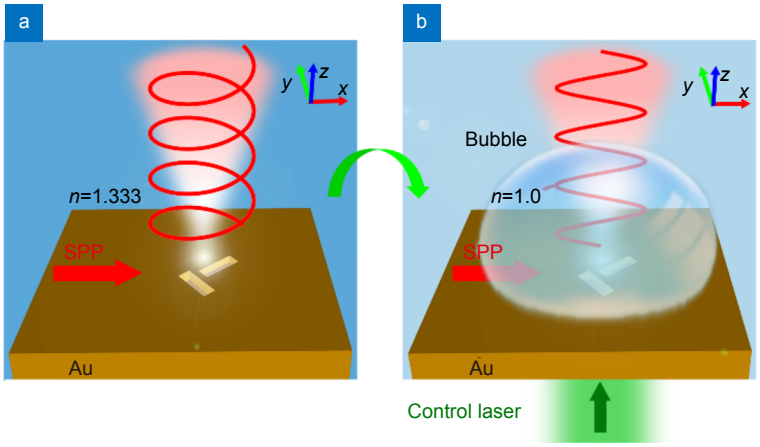

Fig. 1 | (**a**) Circularly polarized emission light as the plasmonic emitter is covered by water (n=1.333). (**b**) Linearly polarized emission light as the plasmonic emitter is covered by a bubble (n=1.0) induced with a control laser beam.

powers of the emission light from the two antennas can be adjusted by the structural parameters of the two antennas[13,15]. The phase difference (φ) of the emission light from the two antennas can be written as[15]

$$\varphi = k_0 n_{\text{eff}}(n) \times s_x + (\varphi_2 - \varphi_1) + \varphi_t \,, \qquad (1)$$

where $k_0=2\pi/\lambda$ is a vacuum wave-vector; $n_{\text{eff}}(n)=[\varepsilon_{\text{metal}}\times n^2/(\varepsilon_{\text{Au}}+n^2)]^{1/2}$ is the effective refractive index of the SPP mode confined on the metal surface, and it is sensitive to the refractive index (n) of the surrounding medium[29,35]; $\varepsilon_{\text{metal}}$ is a relative permittivity of metal; φ_1 and φ_2 are the scattering phases of the two antennas, respectively; φ_t is the phase propagating through the first antenna; s_x is the separation of the two nanogroove antennas along the x-axis. The emission polarization state of the plasmonic emitter is determined by the value of φ. For $\varphi=\pi/2+m\pi$ (m being an integer), the emission light is circularly polarized (Fig. 1(a)). When the phase difference is changed to be $\varphi=m'\pi$ (m' being an integer), the emission light is switched to be linearly polarized (Fig. 1(b)). Hence, the emission polarization state from the plasmonic emitter (Fig. 1(a)) can be switched by changing the refractive index (n) of the covered medium on the metal surface, as shown in Fig. 1. To realize this polarization-switching phenomenon, the smallest phase change is $\Delta\varphi=\pi/2$. For an ultra-small plasmonic emitter with $s_x < \lambda$, a large index variation ($\Delta n>0.25$) is need to obtain $\Delta\varphi=\pi/2$ based on Eq. (1). The smaller the device size (s_x) is, the larger the index variation (Δn) is required. Such a large index variation is difficult to be achieved by using electro-optical[33,34,37,38], thermo-optical[39,40], magneto-optical[32,41], and all-optical[29,42–44] tuning methods. Herein, we propose to use a control laser to induce a bubble (n=1.0) in water (n=1.333)[35], and a large index variation as high as Δn=0.333 is obtain to realize efficient polarization switching.

Simulation and discussion

To validate that this large index variation (Δn=0.333) can realize polarization switching in our designed plasmonic emitter, the properties of the emission light from one nanogroove antenna covered by different mediums with refractive indices of n=1.333 and n=1.0 are first studied by employing the finite element method of Comsol Multiphysics. The schematic of a nanogroove antenna is displayed in Fig. 2(a). The length, width, depth, and tilting

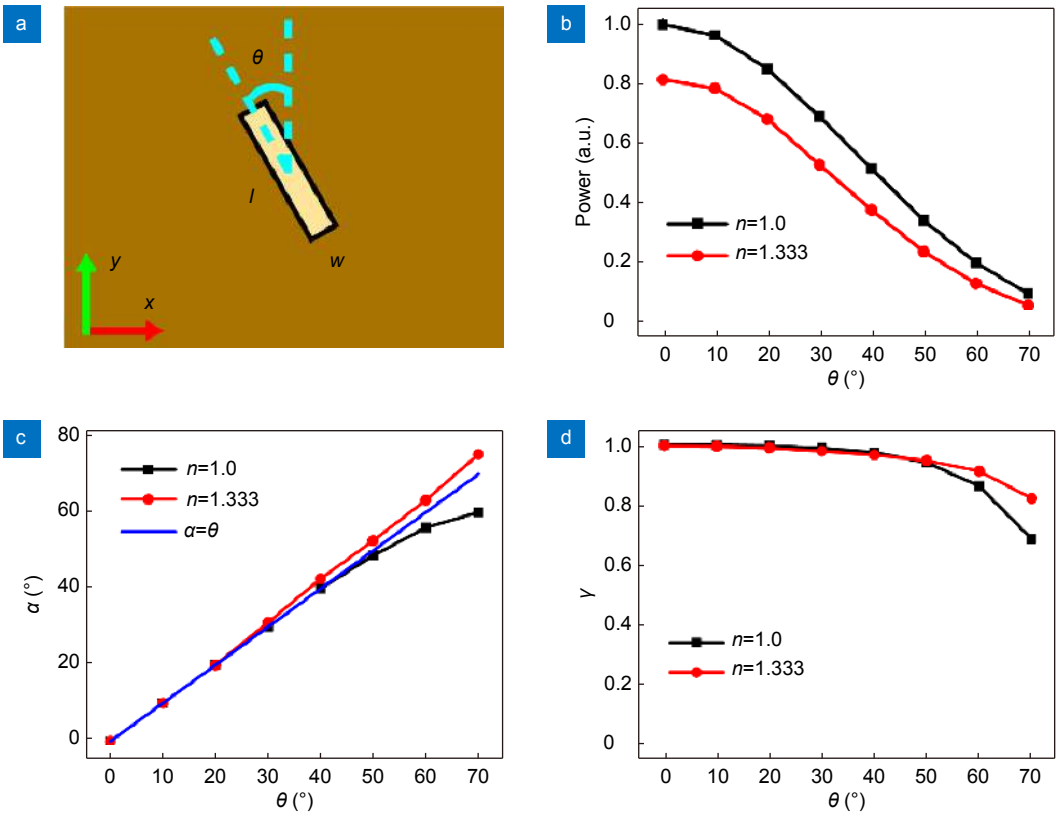

Fig. 2 | (**a**) Structure diagram and geometry parameters of a nanogroove antenna. Simulated (**b**) powers, (**c**) polarization orientation angles, and (**d**) degrees of linear polarization (D_p) of the emission lights from one nanogroove antenna when the antenna is covered by different mediums with refractive indices of n=1.333 (red lines) and n=1.0 (black lines).

angle of the nanogroove are l, w, d, and θ, respectively. In simulations, the metal film is set as gold, and its relative permittivity is ε_{Au}=−32.78+2.00i at a vacuum wavelength of λ=900 nm[45]. By varying the tilting angle of the nanogroove antenna, the properties (power, polarization orientation angle, and degree of linear polarization)[13,15] of the emission light from the nanogroove antenna are calculated at λ=900 nm when n=1.0 (black lines) or n=1.333 (red lines), as displayed in Fig. 2(b–d). The simulation method and the definition of the polarization orientation angle and degree of linear polarization can be found in our previous works[13,15]. Here, the length, width, and depth of the nanogroove are fixed to be l=400 nm, w=100 nm, and d=200 nm, respectively. Further simulation results show that the resonant wavelengths of the antenna covered by different mediums with refractive indices of n=1.333 and n=1.0 are λ'≈970 nm and λ''≈880 nm, respectively. Similar resonant spectra of the nanogroove antenna can be found in our previous works[13,15]. Hence, the difference of the powers of the emission light from the nanogroove antenna covered by a medium with a refractive index of n=1.0 and a medium with a refractive index of n=1.333 at the working wavelength λ=900 nm is small, as shown in Fig. 2(b). By slightly adjusting the working wavelength or structural parameters of the nanogroove antenna, the power difference can become smaller.

For θ<50°, the polarization orientation angles of the emission light from the antenna covered by a medium with a refractive index of n=1.0 are approximately equal to that covered by a medium with a refractive index of n=1.333, as shown in Fig. 2(c). The reason is that the polarization orientation angle of the emission light is mainly determined by the tilting angle of the antenna[13]. For θ=45°, the polarization orientation angles of the emission light from the antenna covered by different mediums with refractive indices of n=1.333 and n=1.0 are both approximately α=45°. Moreover, the degrees of linear polarization (γ)[13,15] of the emission light from the antenna covered by different mediums with refractive indices of n=1.333 and n=1.0 are nearly the same, and they are both greater than 0.9 for θ<50°, as shown in Fig. 2(d). This indicates that the degrees of linear polarization of the emission light from the nanogroove antenna remain high for n=1.333 and n=1.0.

The above simulations show that the refractive index of the covered medium (n=1.333 or n=1.0) has little influence on the polarization orientation angle and degree of linear polarization of the emission light from the nanogroove antenna. Based on Eq. (1), the refractive index of the covered medium (n=1.333 or n=1.0) has large influence on the phase difference (φ) of the emission light from the two antennas in Fig. 1. To test our analysis, the polarization states of the plasmonic emitter (Fig. 3(a)) covered by different mediums with refractive indices of n=1.333 and n=1.0 are simulated. Figure 3(a) shows the top view of the two orthogonal subwavelength metallic nanogroove antennas (θ_1=45° and θ_2=−45°) as well as the structural parameters. When the structural parameters are l=400 nm, w=100 nm, d_1=200 nm, d_2=180 nm, s_y=300 nm, and s_x=120 nm, the simulation results of the polarization states of the emission light are displayed in Fig. 3(b, c). It is observed that the emission light from the plasmonic emitter is circularly polarized for n=1.333, as shown by the red line in Fig. 3(b). The degrees of linear polarization is calculated to be γ=0.03 (Fig. 3(c)). When the refractive index of the covered medium is changed to be n=1.0, the emission light from the plasmonic emitter turns to be linearly polarized, as shown by the black line in Fig. 3(b). In this case, the degrees of linear polarization is calculated to be γ'=0.74 (Fig. 3(c)). The polarization orientation angle of the linearly polarized emission light from the plasmonic emitter is α_{air}≈350°. The reason is that the intensity of the emission light from the upper nanogroove antenna is greater than that from the lower nanogroove antenna. Hence, by changing the refractive index of the covered medium from n=1.333 to n=1.0, the emission polarization of the plasmonic emitter is switched from near-circular polarization to near-linear polarization ($|\Delta\gamma|$>0.5) in a wavelength range from λ=870 nm to λ=980 nm, as shown in Fig. 3(c).

Experiment and discussion

To test our proposal experimentally, the plasmonic emitter consisting of two nanogroove antennas is fabricated by a focused ion beams (FIB) method on a 450 nm thick gold film, which is deposited on a glass substrate with a 30 nm thick titanium adhesion layer[13]. Here, three plasmonic emitters with the same geometrical parameters are fabricated in a column with a separation of about 5 μm, as shown on the right side of Fig. 4(a). A slit with a length of 20 μm and a width of 100 nm is fabricated on the gold film to excite the SPP mode on the front gold surface under the back-side illumination[46], as shown by the left side of Fig. 4(a). The separation of the slit and plasmonic emitters is 15 μm. The zoomed-in scanning

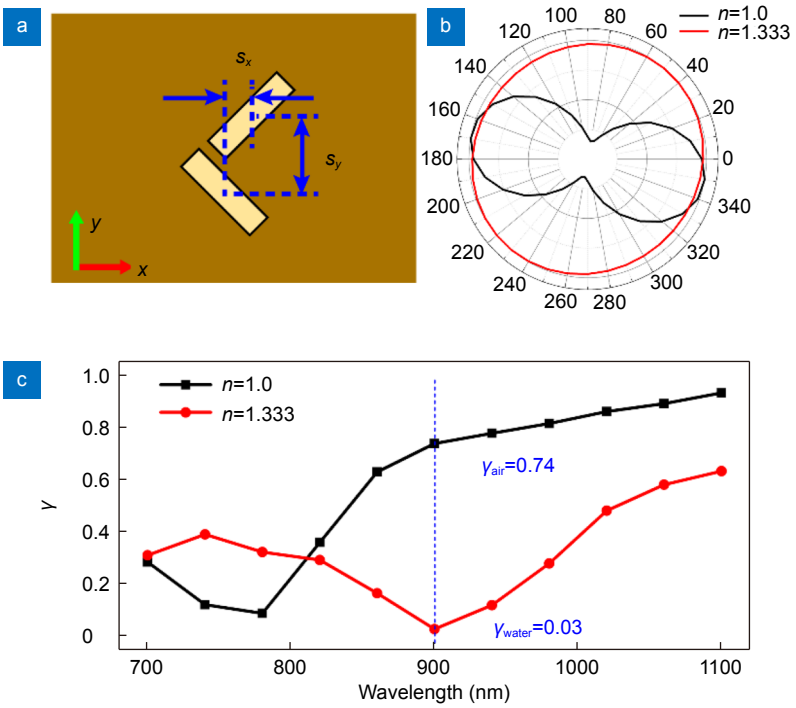

Fig. 3 | (**a**) Structure diagram and geometry parameters of the plasmonic emitter. (**b**) Polar plot of the simulated intensity of the emission light from the plasmonic emitter as a function of the polarization angle for n=1.333 (red line) or n=1.0 (black line) at λ=900 nm. (**c**) Degrees of linear polarization of the emission light from the plasmonic emitter varying with the wavelengths for n=1.333 (red line) or n=1.0 (black line).

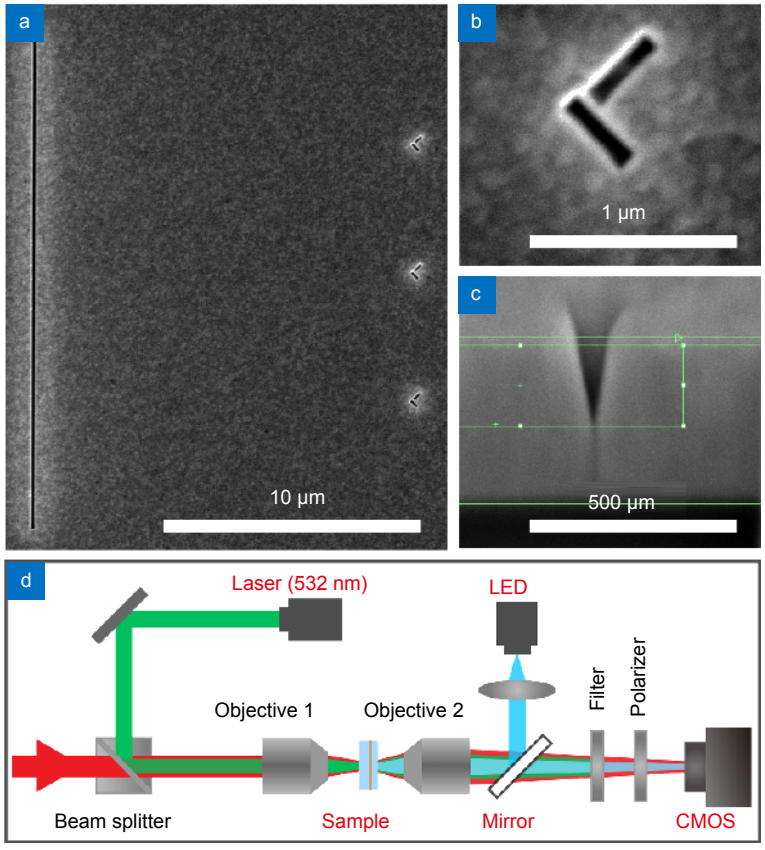

Fig. 4 | (**a**) SEM image of the fabricated structure. (**b**) Zoomed-in SEM image of a plasmonic emitter. (**c**) Cross-section of a nanogroove antenna. The green lines is used to measure the thickness of the gold film and the depth of the nanogroove antenna. (**d**) Schematic of the measurement set-up.

electron microscope (SEM) image of the plasmonic emitter is displayed in Fig. 4(b), and the cross-section of the nanogroove antenna is shown in Fig. 4(c). It is observed that the nanogroove tapers down to the bottom because of the fabrication limit of the FIB method. This deviation affects the resonant wavelength, but it has little influence on the polarization orientation angle and degree of linear polarization of the emission light from the nanogroove antenna. The measured geometrical parameters of the two nanogroove antennas are l≈400 nm, w≈100 nm, d_1≈220 nm, d_2≈160 nm, s_y≈300 nm, and s_x≈120 nm.

Then, a 25 mm×25 mm cover glass is placed above the gold film to form a gap. We drop water into the gap and press the cover glass to get a thin water film (about 10 μm). The samples are measured by using a home-built microscopy imaging system, as shown in Fig. 4(d). A p-polarized monochromatic light with a wavelength of λ (red beam in Fig. 4(d)) is focused on the substrate by a microscope objective (Mitutoyo 20× and NA=0.4). The SPP mode on the front metal surface is excited and then impinges the plasmonic emitters. The emission light from the plasmonic emitters is collected by another objective (Mitutoyo 100× and NA=0.5). After passing a long-pass filter (cut-off wavelength=600 nm) and a polarizer, the emission light is imaged onto a complementary metal-oxide-semiconductor transistor (CMOS). A control laser beam (green beam in Fig. 4(d)) with a wavelength of λ_c=532 nm is also focused on the structure from the backside. The gold film absorbs the control laser, and the water on the water-gold interface is heated, inducing a bubble under a critical intensity of the control laser beam. A white light-emitting diode (LED) illuminates the structure from the front side to monitor the bubble emerging on the gold surface. The long-pass filter (600 nm) is used to block the pump light, and the polarizer is used to collect CMOS images at different polarizer angles.

The polarization states of the emission light from the plasmonic emitter are investigated when the plasmonic emitter is covered by air or water (without the control light). When the plasmonic emitter is covered by air (n=1.0), the captured CMOS image is displayed in Fig. 5(a) (at an incident wavelength of λ=900 nm). It is observed that there are three bright spots on the right side of Fig. 4(a), which indicates that the confined SPP mode is emitted into the free-radiation field by the plasmonic emitters. The left bright line is the directly transmitted light from the 100-nm-wide slit. By rotating the polarizer in front of the CMOS, the optical images of the

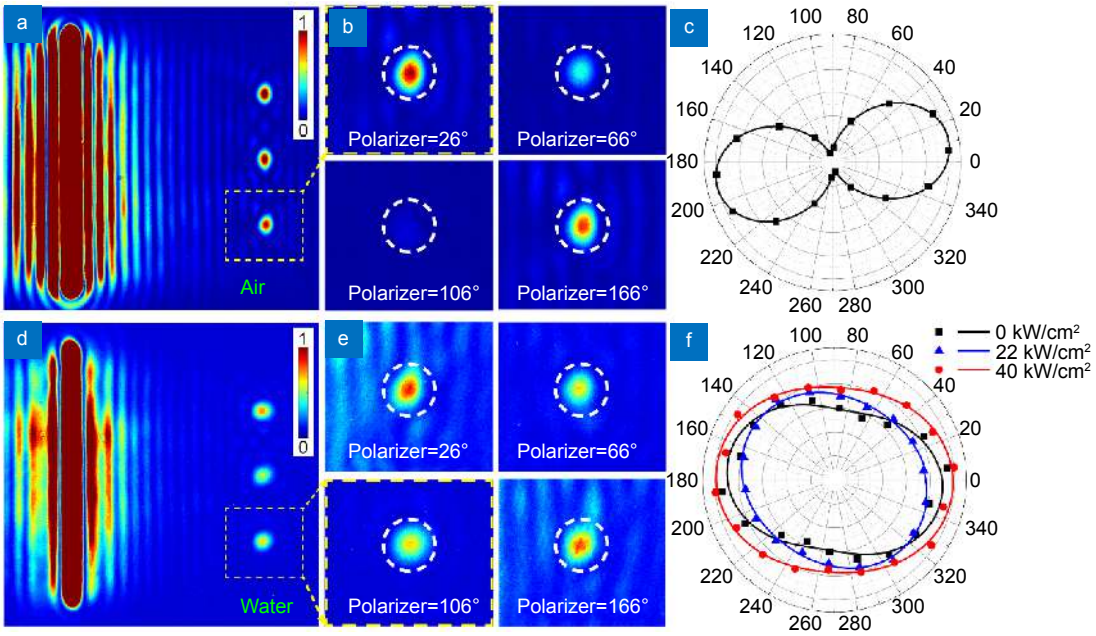

Fig. 5 | (**a**) Captured CMOS image of the sample in air. (**b**) CMOS images of the emission light from the plasmonic emitter [denoted by the yellow dashed square in (a)] at different polarizer angles. (**c**) Polar plot of the measured intensities of the emission light from the plasmonic emitter in air by rotating the polarizer. (**d**) Captured CMOS image of the sample in water. (**e**) CMOS images of the emission light from the plasmonic emitter [yellow dashed box in (d)] at different polarizer angles. (**f**) Polar plot of the measured intensities of the emission light from the plasmonic emitter by rotating the polarizer at different pump intensities.

emission light from the plasmonic emitter (yellow dashed box in Fig. 5(a)) are shown in Fig. 5(b). When the polarizer angle is 106°, the emission spot (in the areas of the white dashed circles in Fig. 5(b)) is invisible, revealing the linear polarization state for the emission light. The measured intensities of the emission light from the plasmonic emitter (yellow dashed box in Fig. 5(a)) at different polarizer angles are shown in Fig. 5(c), which also reveals the linearly polarized light. The polarization orientation angle and degree of linear polarization of the linearly polarized emission light from the plasmonic emitter in air are $\alpha_{air}\approx10°$ and $\gamma_{air}\approx0.86$, respectively. The polarization orientation angle is different from that in the simulation (Fig. 3(b)). This difference originates from that the intensity of the emission light from the upper nanogroove antenna becomes smaller than that from the lower nanogroove antenna. Because of the fabrication limit of FIB, the structural parameters of the nanogroove antennas (especially the depth of the nanogroove) in the experiment deviate from that in the simulation. Hence, the scattered light of the upper groove is greater than that of the lower groove in the simulation but reversed in the experiment.

When the plasmonic emitter is covered by a water film (n=1.333), the captured CMOS image of the sample is shown in Fig. 5(d). Figure 5(e) shows the optical images of the emission light from the plasmonic emitter (yellow dashed box in Fig. 5(d)) at different polarizer angles. It is observed that the emission spots (in the areas of the white dashed circles in Fig. 5(e)) have nearly the same brightness, indicating the elliptically polarized light. By rotating the polarizer, the measured intensities of the emission light from the plasmonic emitter are displayed by the black symbols in Fig. 5(f). The black line is a fitting curve, which also reveals that the emission light is elliptically polarized. The degree of linear polarization of the elliptically polarized light is $\gamma_{water}\approx0.20$, which is greater than $\gamma'_{water}\approx0.03$ in the simulation. This difference between the experiment and simulation is attributed to the deviation of the structural parameters of the antenna (especially the depth of the antenna) in the FIB fabrication process and in the simulation. Hence, the emission polarization states of the emission light from the plasmonic emitter are quite different when the plasmonic emitter is covered by air (n=1.0) and water (n=1.333).

Next, the dynamical switching of the emission polarization of the plasmonic emitter is experimentally demonstrated by using a control laser beam to induce a microbubble in water. Under a small control intensity at λ_c=532 nm (<44 kW/cm^2), the nanobubbles emerge in water, resulting in a small equivalent index variation ($|\Delta n|$<0.05)[35]. The nano-bubble size is several nanometers, and the nano-bubbles distribute at the hot spots of the nanogroove (induced by the control laser of λ=532 nm). Hence, this small index variation has little influence on the emission polarization of the plasmonic emitter because of the ultra-small size of the plasmonic emitter (~0.4 λ^2), and the measured results are depicted by the blue triangle and red circle symbols in Fig. 5(f) under two different control intensities of 22 kW/cm^2 and 40 kW/cm^2. The blue and red lines are fitting curves. The change of the degree of linear polarization is $|\Delta\gamma|\leq0.09$ for I_p<40 kW/cm^2.

When the intensity of the control laser beam increases to I_p=44 kW/cm^2, a microbubble (n_{bubble}=1.0)[35] emerges in water (n_{water}=1.333), and it covers the whole structure on the metal surface, as shown in Fig. 6(a). Then, we decrease the intensity of the control laser beam a little, the bubble dose not collapse and keeps unchanged below a laser threshold power because of thermal equilibrium of this system[47]. The micro-bubble size is more than one micrometer, and the micro-bubble distributes on the metal surface. Hence, the adjacent medium on the metal surface is changed from water to the microbubble. The controlling intensity is much smaller than that in the previous all-optical tuning method[4,48,49]. The large index variation of $|\Delta n|$=0.333 greatly changes the phase difference (especially $k_0 n_{eff}\times s_x$) of the emission light from the two nanogroove antennas based on Eq. (1). In this case, the captured CMOS images at different polarizer angles are displayed in Fig. 6(b). At a polarizer angle of 106°, the emission spot (in the areas of the white dashed circles in Fig. 6(b)) becomes invisible, just like the case when the plasmonic emitter is covered by air (Fig. 5(b)). By rotating the polarizer, the measured intensities of the emission light from the plasmonic emitter are shown by the red symbols in Fig. 6(c), where the red line is a fitting curve. It is observed that the emission light from the plasmonic emitter in the microbubble is linearly polarized ($\alpha_{bubble}\approx10°$ and $\gamma_{bubble}\approx0.86$), which is consistent with the emission polarization when the plasmonic emitter is covered by air (black symbols and black line in Fig. 5(c)). This further verifies that the refractive index of the bubble is 1.0. Compared to the results in water (blue symbols and blue line in Fig. 6(c)), the change of the

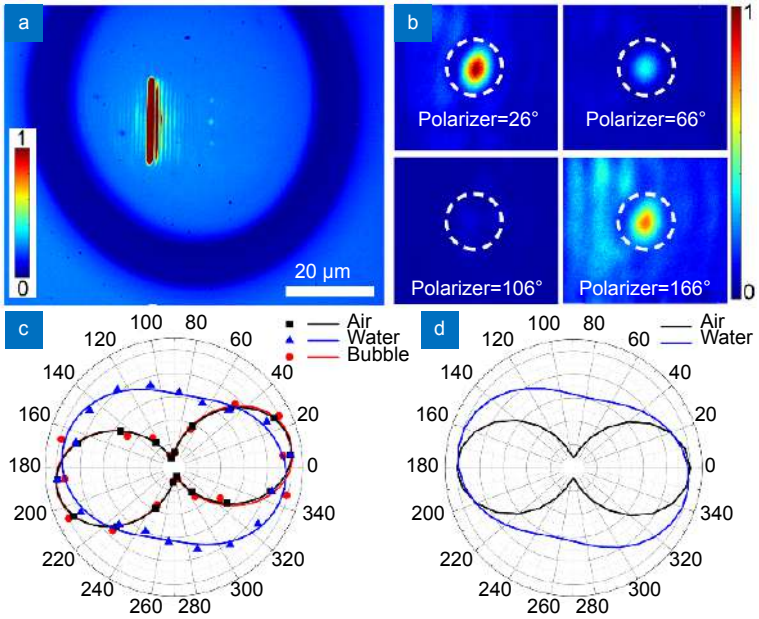

Fig. 6 | (**a**) CMOS image of a microbubble, which covers the sample. (**b**) CMOS images of the emission light from the plasmonic emitter in the microbubble at different polarizer angles. (**c**) Polar plot of the measured intensities of the emission light from the plasmonic emitter by rotating the polarizer in air (black), water (blue), and bubble (red). (**d**) Polar plot of the simulated intensities of the emission light from the plasmonic emitter at different polarizer angles when the plasmonic emitter is covered by air (black), water (blue), and bubble (red). The result in air is the same as that in the bubble, so the red line is covered by the black line.

degree of linear polarization reaches up to $\Delta\gamma\approx0.66$ due to a large index variation ($|\Delta n|=0.333$). The simulation results are displayed in Fig. 6(d), and the experiment data (Fig. 6(c)) agree with the simulation results. Therefore, the plasmonic polarization-switchable emitter is achieved at nanometer scales by using a low-intensity laser beam to induce a microbubble in water. The switching time is smaller than 1 second[47]. It is possible to reversibly switch the emission polarization by switching off the control laser or moving the control laser away from the emitter[47].

Conclusions

In summary, by using a control laser beam to induce a microbubble in water, the emission polarization of an ultra-small plasmonic emitter was experimentally switched at nanometer scales. Simulations showed that the emission light from the designed plasmonic emitter exhibited different polarization states (linear polarization state and circular polarization state) when the plasmonic emitter is covered by different media with refractive indices of $n=1.333$ and 1.0. By using a control laser beam above a critical intensity, a microbubble emerged in water on the metal surface. Because of the large index variation of $|\Delta n|=0.333$ brought by the laser-induced bubble, the emission light from the plasmonic emitter changed from an elliptical polarization state in water to a linear polarization state in a microbubble. The separation of the two antennas was only $s_x=120$ nm, and the footprint was approximately $0.4\lambda^2$. This strategy could also be used to dynamically switch the emission polarization of single-photon sources[50] and other hybrid nanostructures[51,52]. This ultra-small polarization-switchable plasmonic emitter might increase flexibilities and communication capacities in inter-chip optical communications and quantum communications.

References

1. Gramotnev DK, Bozhevolnyi SI. Plasmonics beyond the diffraction limit. *Nat Photonics* **4**, 83–91 (2010).
2. Wang WH, Yang Q, Fan FR, Xu HX, Wang ZL. Light propagation in curved silver nanowire plasmonic waveguides. *Nano Lett* **11**, 1603–1608 (2011).
3. Cohen M, Zalevsky Z, Shavit R. Towards integrated nanoplasmonic logic circuitry. *Nanoscale* **5**, 5442–5449 (2013).
4. Chen JJ, Gan FY, Wang YJ, Li GZ. Plasmonic sensing and modulation based on fano resonances. *Adv Opt Mater* **6**, 1701152 (2018).
5. Ma JX, Zeng DZ, Yang YT, Pan C, Zhang L et al. A review of crosstalk research for plasmonic waveguides. *Opto-Electron Adv* **2**, 180022 (2019).
6. Berini P, De Leon I. Surface plasmon–polariton amplifiers and lasers. *Nat Photonics* **6**, 16–24 (2012).
7. Yang Y, Miller OD, Christensen T, Joannopoulos JD, Soljačić M. Low-loss plasmonic dielectric nanoresonators. *Nano Lett* **17**, 3238–3245 (2017).
8. Zhang YF, Wang HM, Liao HM, Li Z, Sun CW et al.

Unidirectional launching of surface plasmons at the sub-wavelength scale. *Appl Phys Lett* **105**, 231101 (2014).
9. Haffner C, Chelladurai D, Fedoryshyn Y, Josten A, Baeuerle B et al. Low-loss plasmon-assisted electro-optic modulator. *Nature* **556**, 483–486 (2018).
10. Paolo B, Huang JS, Hecht B. Nanoantennas for visible and infrared radiation. *Rep Prog Phys* **75**, 024402 (2012).
11. Dregely D, Lindfors K, Lippitz M, Engheta N, Totzeck M et al. Imaging and steering an optical wireless nanoantenna link. *Nat Commun* **5**, 4354 (2014).
12. Alù A, Engheta N. Wireless at the nanoscale: optical interconnects using matched nanoantennas. *Phys Rev Lett* **104**, 213902 (2010).
13. Sun CW, Li HY, Gong QH, Chen JJ. Plasmonic polarization-rotating emitters with metallic nanogroove antennas. *Adv Opt Mater* **5**, 1700510 (2017).
14. Wang JW, Bonneau D, Villa M, Silverstone JW, Santagati R et al. Chip-to-chip quantum photonic interconnect by path-polarization interconversion. *Optica* **3**, 407–413 (2016).
15. Gan FY, Li HY, Chen JJ. Tailoring the emission polarization with metasurface-based emitters designed on a plasmonic ridge waveguide. *Nanoscale* **11**, 7140–7148 (2019).
16. Curto AG, Taminiau TH, Volpe G, Kreuzer MP, Quidant R et al. Multipolar radiation of quantum emitters with nanowire optical antennas. *Nat Commun* **4**, 1750 (2013).
17. Geisler P, Razinskas G, Krauss E, Wu XF, Rewitz C et al. Multimode plasmon excitation and *in situ* analysis in top-down fabricated nanocircuits. *Phys Rev Lett* **111**, 183901 (2013).
18. Kim J, Roh YG, Cheon S, Kim UJ, Hwang SW et al. Directional radiation of Babinet-inverted optical nanoantenna integrated with plasmonic waveguide. *Sci Rep* **5**, 11832 (2015).
19. Ren MX, Chen M, Wu W, Zhang LH, Liu JK et al. Linearly polarized light emission from quantum dots with plasmonic nanoantenna arrays. *Nano Lett* **15**, 2951–2957 (2015).
20. Lin J, Mueller JPB, Wang Q, Yuan GG, Antoniou N et al. Polarization-controlled tunable directional coupling of surface plasmon polaritons. *Science* **340**, 331–334 (2013).
21. Vercruysse D, Zheng XZ, Sonnefraud Y, Verellen N, Di Martino G et al. Directional fluorescence emission by individual v-antennas explained by mode expansion. *ACS Nano* **8**, 8232–8241 (2014).
22. Hancu IM, Curto AG, Castro-López M, Kuttge M, van Hulst NF. Multipolar interference for directed light emission. *Nano Lett* **14**, 166–171 (2014).
23. Curto AG, Volpe G, Taminiau TH, Kreuzer MP, Quidant R et al. Unidirectional emission of a quantum dot coupled to a nanoantenna. *Science* **329**, 930–933 (2010).
24. Dregely D, Taubert R, Dorfmüller J, Vogelgesang R, Kern K et al. 3D optical Yagi–Uda nanoantenna array. *Nat Commun* **2**, 267 (2011).
25. Obelleiro F, Taboada JM, Solís DM, Bote L. Directive antenna nanocoupler to plasmonic gap waveguides. *Opt Lett* **38**, 1630–1632 (2013).
26. Guo YH, Pu MB, Zhao ZY, Wang YQ, Jin JJ et al. Merging geometric phase and plasmon retardation phase in continuously shaped metasurfaces for arbitrary orbital angular momentum generation. *ACS Photonics* **3**, 2022–2029 (2016).
27. Li ZP, Shegai T, Haran G, Xu HX. Multiple-particle nanoantennas for enormous enhancement and polarization control of light emission. *ACS Nano* **3**, 637–642 (2009).
28. Zhao Y, Alù A. Manipulating light polarization with ultrathin plasmonic metasurfaces. *Phys Rev B* **84**, 205428 (2011).
29. Chen JJ, Li Z, Yue S, Gong QH. Highly efficient all-optical control of surface-plasmon-polariton generation based on a compact asymmetric single slit. *Nano Lett* **11**, 2933–2937 (2011).
30. Pacifici D, Lezec HJ, Atwater HA. All-optical modulation by plasmonic excitation of CdSe quantum dots. *Nat Photonics* **1**, 402–406 (2007).
31. MacDonald KF, Sámson ZL, Stockman MI, Zheludev NI. Ultrafast active plasmonics. *Nat Photonics* **3**, 55–58 (2009).
32. Temnov VV, Armelles G, Woggon U, Guzatov D, Cebollada A et al. Active magneto-plasmonics in hybrid metal–ferromagnet structures. *Nat Photonics* **4**, 107–111 (2010).
33. Haffner C, Heni W, Fedoryshyn Y, Niegemann J, Melikyan A et al. All-plasmonic Mach–Zehnder modulator enabling optical high-speed communication at the microscale. *Nat Photonics* **9**, 525–528 (2015).
34. Ayata M, Fedoryshyn Y, Heni W, Baeuerle B, Josten A et al. High-speed plasmonic modulator in a single metal layer. *Science* **358**, 630–632 (2017).
35. Gan FY, Wang YJ, Sun CW, Zhang GR, Li HY et al. Widely tuning surface plasmon polaritons with laser-induced bubbles. *Adv Opt Mater* **5**, 1600545 (2017).
36. Zhao CL, Liu YM, Zhao YH, Fang N, Huang TJ. A reconfigurable plasmofluidic lens. *Nat Commun* **4**, 2305 (2013).
37. Dickson W, Wurtz GA, Evans PR, Pollard RJ, Zayats AV. Electronically controlled surface plasmon dispersion and optical transmission through metallic hole arrays using liquid crystal. *Nano Lett* **8**, 281–286 (2008).
38. Buchnev O, Ou JY, Kaczmarek M, Zheludev NI, Fedotov VA. Electro-optical control in a plasmonic metamaterial hybridised with a liquid-crystal cell. *Opt Express* **21**, 1633–1638 (2013).
39. Gosciniak J, Markey L, Dereux A, Bozhevolnyi SI. Efficient thermo-optically controlled Mach-Zhender interferometers using dielectric-loaded plasmonic waveguides. *Opt Express* **20**, 16300–16309 (2012).
40. Cetin AE, Mertiri A, Huang M, Erramilli S, Altug H. Thermal tuning of surface plasmon polaritons using liquid crystals. *Adv Opt Mater* **1**, 915–920 (2013).
41. Wurtz GA, Hendren W, Pollard R, Atkinson R, Le Guyader LL et al. Controlling optical transmission through magneto-plasmonic crystals with an external magnetic field. *New J Phys* **10**, 105012 (2008).
42. Zhang XP, Sun BQ, Hodgkiss JM, Friend RH. Tunable ultrafast optical switching via waveguided gold nanowires. *Adv Mater* **20**, 4455–4459 (2008).
43. Chen JJ, Li Z, Zhang X, Xiao JH, Gong QH. Submicron bidirectional all-optical plasmonic switches. *Sci Rep* **3**, 1451 (2013).
44. Sim S, Jang H, Koirala N, Brahlek M, Moon J et al. Ultra-high modulation depth exceeding 2, 400% in optically controlled topological surface plasmons. *Nat Commun* **6**, 8814 (2015).
45. Johnson PB, Christy RW. Optical constants of the noble metals. *Phys Rev B* **6**, 4370–4379 (1972).
46. Chen JJ, Li Z, Yue S, Gong QH. Efficient unidirectional generation of surface plasmon polaritons with asymmetric single-nanoslit. *Appl Phys Lett* **97**, 041113 (2010).
47. Li GZ, Jia ST, Yang H, Chen JJ. Direction-controllable plasmonic color scanning by using laser-induced bubbles. *Adv Funct Mater* **31**, 2008579 (2021).
48. Ono M, Hata M, Tsunekawa M, Nozaki K, Sumikura H et al.

Ultrafast and energy-efficient all-optical switching with graphene-loaded deep-subwavelength plasmonic waveguides. *Nat Photonics* **14**, 37–43 (2020).

49. Niu XX, Hu XY, Lu CC, Sheng Y, Yang H et al. Broadband dispersive free, large, and ultrafast nonlinear material platforms for photonics. *Nanophotonics* **9**, 4609–4618 (2020).
50. Zhang GR, Gu Y, Gong QH, Chen JJ. Symmetry-tailored patterns and polarizations of single-photon emission. *Nanophotonics* **9**, 3557–3565 (2020).
51. He JJ, Zheng W, Ligmajer F, Chan CF, Bao ZY et al. Plasmonic enhancement and polarization dependence of nonlinear upconversion emissions from single gold nanorod@SiO_2@CaF_2:Yb^{3+}, Er^{3+} hybrid core-shell-satellite nanostructures. *Light Sci Appl* **6**, e16217 (2017).
52. Li GC, Zhang YL, Jiang J, Luo Y, Lei DY. Metal-substrate-mediated plasmon hybridization in a nanoparticle dimer for photoluminescence line-width shrinking and intensity enhancement. *ACS Nano* **11**, 3067–3080 (2017).

Acknowledgements

This work was supported by the National Key Research and Development Program of China (2018YFA0704401), the Beijing Natural Science Foundation (Z180015), and the National Natural Science Foundation of China (61922002 and 91850103).

Competing interests

The authors declare no competing financial interests.